RESEARCH ARTICLE

Key Points:
- DSD broadening depends on the mixing time scale and the LWC after mixing
- DSD broadening increases substantially as the evaporation time scale decreases
- We related the fraction of droplets that totally evaporate to two DSD parameters

Effects of entrainment and mixing on droplet size distributions in warm cumulus clouds

Merja H. Tölle[1,2] and Steven K. Krueger[3]

[1]Institute of Coastal Research, Helmholtz-Zentrum Geesthacht, Geesthacht, Germany, [2]Now at Department of Bioclimatology, University of Göttingen, Göttingen, Germany, [3]Department of Atmospheric Sciences, University of Utah, Salt Lake City, Utah, USA

Abstract A long-standing problem in cloud physics is the broadening of the cloud droplet spectrum in warm cumulus clouds. To isolate the changes of the droplet size distribution (DSD) due to entrainment and turbulent mixing, we used the Explicit Mixing Parcel Model (EMPM). The EMPM explicitly represents spatial variability due to entrainment and turbulent mixing down to the smallest turbulence scales in a one-dimensional domain. Several thousand individual droplets evolve by condensation or evaporation according to their local environments. We used EMPM results to characterize the evolution of the DSD due to entrainment and isobaric mixing for a wide range of conditions in a 20 m domain, including variations in entrained environmental air fraction, the turbulence dissipation rate, the size of the entrained blobs, and the relative humidity of the entrained air. We found that the broadening of the DSD due to entrainment and isobaric mixing for a specific value of the entrained air relative humidity depends only on the eddy mixing time scale and the LWC after mixing. Broadening increases substantially as the evaporation time scale decreases due to decreasing relative humidity of the entrained air. Our results also show that it is possible to parameterize the effects of entrainment and mixing on the droplet number concentration. The comprehensive results obtained for one set of values of entrained air relative humidity, droplet size, and droplet concentration should be extended to other values.

1. Introduction

A ubiquitous cloud regime over much of the subtropical oceans is shallow cumulus convection. These trade wind cumuli typically are dominated by warm rain processes. Characterizing their properties is important for understanding the hydrological cycle, the net radiative forcing [*Morrison and Grabowski*, 2007], and the global energy balance and climate [*Stevens and Feingold*, 2009]. At the smallest microphysical scales, the most fundamental problem—recognized for over half a century—is explaining the rapid onset of precipitation in these clouds. Any proposed mechanism must account for growth from condensation nuclei to raindrops in about 15–20 min [*Johnson*, 1993]. The short time for the rain development requires the droplet size spectra to be broad enough for droplets to have a high rate of coalescence growth.

The mechanisms responsible for the rapid formation of rain in warm clouds have yet to be adequately explained, and this lack of understanding motivated the RICO field campaign [*Rauber et al.*, 2007]. One hypothesis is that large cloud droplets form on giant and ultragiant nuclei and then rapidly grow. Another hypothesis invokes increased collision rates due to nonuniform droplet spatial distributions produced by small-scale turbulence (see review by *Devenish et al.* [2012]). Spectral broadening produced by entrainment and mixing has also been proposed as a mechanism for accelerating coalesence growth [e.g., *Berry and Reinhardt*, 1974; *Blyth*, 1993; *Devenish et al.*, 2012] and is the topic of our study.

Stommel [1947] was the first to recognize that cumulus clouds had to be significantly diluted by environmental air above the cloud base in order to explain their temperature and liquid water content profiles. Subsequent observations and numerical simulations suggest a conceptual picture of entrainment and mixing in cumulus clouds in which large turbulent eddies engulf discrete blobs of environmental air, then stretch and compress the entrained blobs into successively thinner sheets until the Kolmogorov scale is reached and molecular diffusion becomes significant and modifies the local properties of the air. This view is consistent with the mixing process as pictured by *Baker et al.* [1980], who suggested that the time scales for turbulent

mixing and for droplet evaporation determine the impacts of entrainment and mixing on cloud droplet spectra. Inertial-range scaling indicates that the time scale for complete homogenization of an entrained blob initially of size d is $(d^2/\epsilon)^{1/3}$ where ϵ is the dissipation rate. Typical values of d and ϵ in a cumulus cloud are 100 m and 10^{-2} m^2 s^{-3}, respectively. For these values, the mixing time scale is 100 s, which explains why cumulus clouds typically exhibit significant internal structure. When the mixing time scale is much greater than the droplet evaporation time scale (the time for a droplet of a given size to evaporate in the entrained air), some droplets adjacent to unsaturated regions may completely evaporate, while droplets that remain in saturated regions may remain unaffected. This is referred to as inhomogeneous mixing [*Baker et al.*, 1980]. In the limiting situation, called extreme inhomogeneous mixing, some droplets of all sizes are completely evaporated while the rest are unaffected. In this case, the droplet size distribution is not shifted toward smaller sizes, but the droplet number is decreased.

In the opposite limiting case, the mixing time scale is so much smaller than the droplet evaporation time scale that all droplets at a given level in the cloud are, at any time, exposed to identical conditions of supersaturation or undersaturation. In this case, the droplet size distribution is simply shifted toward smaller diameters. *Baker et al.* [1980] called this homogeneous mixing.

The size of a droplet is the result of its "saturation history," the integral of the saturation experienced by the droplet during its lifetime. The saturation histories of all droplets are identical during homogeneous mixing as defined above. Mixing events in which a droplet population experiences a range of saturation histories, yet during which no droplets completely evaporate, do not fall into any of the three mixing scenarios defined above.

To a limited extent, mixing scenarios can be graphically represented on a "mixing diagram" with coordinates cloud droplet number concentration and mean volume diameter [*Burnet and Brenguier*, 2007], and which is described in detail in section 4. Burnet and Brenguier noted that certain lines on the diagram represent "homogeneous" mixing, which occurs when "all droplets collectively contribute to the moistening of the mixture that has been first homogenized by turbulence," while another line represents "inhomogeneous" mixing, for which the mean volume diameter does not change. Burnet and Brenguier's definition of homogeneous mixing (and of the homogeneous mixing line) is less restrictive than the original definition of *Baker et al.* [1980], in that it only requires that no droplets completely evaporate during mixing, while their "inhomogeneous" mixing is the same as Baker et al.'s "extreme inhomogeneous mixing." *Gerber et al.* [2008], *Lehmann et al.* [2009], and *Lu et al.* [2013] all used the same diagram and referred to the "homogeneous mixing" lines on it. Gerber et al. said that when "all drops are exposed to the same subsaturated conditions" it is termed homogeneous mixing, while Lehmann et al. stated that "all droplets will experience nearly the same subsaturation and will shrink toward smaller sizes until equilibrium is reached" in homogeneous mixing, and Lu et al. said that "In the homogeneous mixing scenario, all droplets evaporate simultaneously." These three descriptions resemble Baker et al.'s original definition of homogeneous mixing more than they do Burnet and Brenguier's less restrictive one. For clarity and consistency, we suggest referring to Baker et al.'s original definition of homogeneous mixing as "extreme homogeneous mixing," and Burnet and Brenguier's less restrictive one as "homogeneous mixing." In our view, the terms "homogeneous mixing" and "inhomogeneous mixing" have lost much of their usefulness because they have not been used consistently. To avoid confusion or misinterpretation, we will avoid using them in our study.

As mentioned already, spectral broadening of the DSD produced by entrainment and mixing is the topic of our study. A characterization of the mixing process in terms of the ratio of the mixing and evaporation time scales is not likely to be sufficient to determine the resulting DSD width. The first is related to the entrained blob size and the turbulence dissipation rate, and the second to a characteristic droplet size and the entrained air relative humidity. Missing factors include the droplet number concentration and the entrained air fraction. In a case study of a small, nonprecipitating continental cumulus cloud, *Jensen et al.* [1985] found a general increase in droplet spectral width with increasing fraction of entrained environmental air.

Lehmann et al. [2009] discussed using the Damköhler number, Da, to characterize the mixing process. Da is the ratio of the mixing time scale to the reaction time scale. Lehmann et al. noted that the reaction time scale has sometimes been defined as the phase relaxation time scale (time scale for water vapor mixing ratio to adjust toward saturation for a population of droplets of fixed radius and number concentration in air of specified initial subsaturation) and sometimes as the droplet evaporation time scale. Lehmann et al.

defined a new length scale ("transition length scale") as the eddy mixing length that produces a mixing time scale equal to the reaction time scale (i.e., Da = 1), and hypothesized that mixing with eddy mixing lengths greater than the transition length scale would mix inhomogeneously, and vice versa.

Lu et al. [2013] defined three measures for the degree of inhomogeneous mixing, then compared each measure to the "transition number" (the transition length scale normalized by the Kolmogorov length scale) as obtained from Explicit Mixing Parcel Model simulations for a range of conditions. They found fairly good correlations for cases with ambient relative humidity of 0.66 or less. They also noted that their results could be used to parameterize the degree of inhomogeneous mixing, which is needed by microphysical schemes that predict the number concentration as well the mixing ratio of cloud droplets [e.g., *Jarecka et al.*, 2013].

In order to quantitatively predict the evolution of DSDs due to entrainment and mixing, droplets must grow or evaporate according to their local microphysical environments which can vary on centimeter scales [*Brenguier*, 1993]. The range of scales that must be included in a numerical model to explicitly represent entrainment and mixing is very large for atmospheric flows. For a typical cumulus cloud, the largest length scale is on the order of 1 km, while the smallest eddy size is on the order of 1 mm. Simulating the entire range of motions responsible for entrainment and mixing in a cumulus cloud with a three-dimensional numerical model is extremely demanding computationally and is not feasible now or in the foreseeable future. An alternative to multidimensional simulations is to employ 1-D models with sufficiently high spatial resolution to accurately predict droplet growth in a turbulent environment. The key to obtaining reliable simulations is to use a realistic treatment of turbulent mixing within the 1-D description.

Jensen and Baker [1989] and *Grabowski* [1993] recognized that turbulent deformation and molecular diffusion could both be explicitly represented in a 1-D small-eddy model. Such a model could also predict droplet growth according to the local microphysical environment. In the models developed by *Jensen and Baker* [1989] and *Grabowski* [1993], turbulent deformation is represented by a specified strain rate that continuously increases the scalar gradients. The strain rate represents the effect of an eddy of a specific size. In Jensen and Baker's model, turbulent deformation is modeled as a compressive strain that continuously shrinks the domain. The strain represents the effect of an eddy of the domain size. Grabowski's model includes a constant, uniform strain rate. In neither model are the effects of smaller and larger eddies included. Jensen and Baker applied their model to study the evolution of droplet spectra during isobaric mixing, given an initial distribution of cloudy and clear air. Grabowski used his model to describe the early stages of the isobaric mixing process between a thin cloudy sheet with initial width of 10 cm and cloud-free air.

Based on their model, Jensen and Baker concluded that total evaporation of some droplets is confined to cases that result in low LWC after mixing is completed, that comparatively more droplets totally evaporate when the "turbulence level" (i.e., deformation rate) is low than when it is high, that significant increases in droplet spectral width can occur after just one mixing event, and that the resulting droplet spectra are wider when the turbulence level is low than when it is high. Their results are consistent with neither the classical (or "extreme") homogeneous evaporation hypothesis (since not all droplets experience the same subsaturation history), nor with the extreme inhomogeneous evaporation hypothesis (since all droplets evaporate to some extent). However, the greater the turbulence level, the more closely the evaporation tends toward "extreme" homogeneous characteristics.

Kerstein [1988] developed a mixing model, the linear eddy model, that is similar in basic concept to Jensen and Baker's but incorporates the effects of eddies of all sizes between the Kolmogorov scale and the integral scale in a manner consistent with inertial-range scaling laws. Applications of this model show that it is capable of accurately describing many features of turbulent mixing [e.g., *Kerstein*, 1991].

Krueger et al. [1997] developed the Explicit Mixing Parcel Model (EMPM), which depicts the fine-scale internal structure of a rising parcel in a cumulus cloud using a 1-D domain. The EMPM links the conventional parcel model, which has no internal structure, and multidimensional cloud models, which resolve cloud-scale structure produced by large eddies. In the EMPM, the internal structure evolves as a consequence of a sequence of discrete entrainment events and a 1-D representation of turbulent mixing based on Kerstein's linear eddy model. The EMPM explicitly represents spatial variability due to entrainment and turbulent mixing down to the smallest turbulence scales. *Su et al.* [1998] included the growth of individual droplets according to their local environments in the EMPM and showed that the EMPM reproduced the broad droplet size distributions (DSDs) measured in Hawaiian trade wind cumulus clouds.

Another modeling framework to predict droplet size distributions affected by entrainment and mixing was presented by *Lasher-Trapp et al.* [2005] consisting of a 3-D cloud model coupled with a Lagrangian parcel model that has no internal structure. The cloud model represents turbulent cloud dynamics but parameterizes microphysical processes such as condensation, and the parcel model complements this approach by performing bin-resolved microphysical calculations within the kinematic and thermodynamic constraints established by the cloud model. The parcel model is run along trajectories ending at the same point in the cloud, and each parcel's droplet size distributions are combined at this point to represent the turbulent mixing of the DSDs produced by the different parcel trajectories. The thermodynamic properties along each trajectory, along with the assumed entrained air properties, imply an entrained air fraction, but do not determine the changes in the DSD in this model, in contrast to the EMPM. Therefore, weighted averages of the two extreme mixing scenarios were considered: extreme homogeneous mixing and extreme inhomogeneous mixing. The results replicate some important features of observed DSDs, including large widths and the continued presence of small droplets high in the clouds. These features arise in the calculations from the variability introduced by entrainment, which leads to varying droplet supersaturation histories.

A major uncertainty limiting the predictive power of Lasher-Trapp et al.'s results is that they depend sensitively on the *assumed* nature of the mixing process. When mixing is assumed to occur rapidly in comparison to the time scale of droplet evaporation the central mode produced by adiabatic ascent tends to be preserved, but when mixing is slow, then the main mode is eroded significantly and a new smaller mode dominates. The most realistic distributions appear to be those produced when the mixing has characteristic incorporating aspects of both these extremes.

Bewley and Lasher-Trapp [2011] used the same modeling framework within trade wind cumuli observed during the Rain in Cumulus over the Ocean (RICO) field campaign. The predicted DSDs are as broad as those observed, contain similar numbers of droplets, and are generally in better agreement with the observations when some degree of inhomogeneous droplet evaporation is considered. The variability of the droplet growth histories, resulting primarily from entrainment, appears to explain the magnitude of the observed DSD widths, without representation of other broadening mechanisms.

Another approach to simulate DSD evolution was carried out by *Andrejczuk et al.* [2004]. They performed two 3-D direct numerical simulations (DNS) with grid lengths of $\Delta x = 10^{-2}$ and 0.25×10^{-2} m, for a fixed 0.643^3 m^3 computational domain, to study the sensitivity of the droplet spectral evolution to the initial volume proportion of the cloudy air. Based on their results, they proposed that the evolution of the cloud droplet spectrum during mixing follows a universal path dictated by the turbulent kinetic energy. More recently, *Kumar et al.* [2013] performed DNSs with grid sizes of 1 mm and volumes of 0.128^3, 0.256^3, and 0.512^3 m^3. to study entrainment and mixing and at the boundary of a cloud. They coupled the Eulerian description of the turbulent velocity and water vapor fields with a Lagrangian ensemble of cloud water droplets that can each grow and shrink by condensation and evaporation. In their DNSs, the turbulence is not driven by buoyancy effects as in similar studies (such as *Andrejczuk et al.* [2006]), but by a volume forcing that mimics a cascade of kinetic energy from larger scales, and therefore are ideally suited to serve as benchmark simulations for evaluating the EMPM. Individual droplets grow or shrink according to their local environments in both DNS and the EMPM. However, DNS can simulate only small volumes, less than 1 m^3, whereas the EMPM can represent larger regions, up to hundreds of meters in extent, because it is 1-D. DNS can, however, include the (small scale) coupling between droplet evaporation and turbulence dynamics.

In this study, we use the EMPM to investigate how entrainment and isobaric mixing affect the broadening of droplet spectra. The analyses of EMPM results address a fundamental difficulty that the large-eddy simulation (LES) approach faces when attempting to represent the effects of entrainment and mixing on droplet microphysics, which is representing the subgrid-scale variability of subsaturation and its impact on droplet size distribution evolution. As a step toward better understanding the effects of entrainment and mixing on droplet spectra in cumulus clouds, we investigated the effects due to isobaric mixing of environmental air entrained in a single event. We used the EMPM results to characterize the evolution of the DSD due to entrainment and isobaric mixing for a wide range of conditions in a 20 m domain, including variations in entrained environmental air fractions, the turbulence dissipation rate, the size of the entrained blobs, and the relative humidity of the entrained air. The remainder of this paper is organized as follows: Mixing and evaporation time scales are reviewed in section 2, a description of the EMPM and the parameters used in the simulations is provided in section 3, simulated bulk microphysical changes due to isobaric mixing are

described using the mixing diagram in section 4, and the simulated effects of entrainment and mixing on the DSD are presented in section 5. Finally, section 6 contains the conclusions.

2. Mixing and Evaporation Time Scales

The statistical properties of DSDs after entrainment and isobaric mixing are affected by the mixing process, in particular, by the variations in the length of time that a droplet is exposed to subsaturated air and thereby produces variability among the droplet saturation histories. Some aspects of the mixing process itself can be characterized by time scales of mixing and evaporation. *Jensen and Baker* [1989], *Lehmann et al.* [2009], *Devenish et al.* [2012], and *Kumar et al.* [2013] include extensive descriptions and discussions of the various time scales that have been proposed. In this section, we define the time scales that we will use, and calculate them from EMPM simulations of two mixing scenarios.

2.1. τ_{RH}

A time scale, τ_{RH}, for the change of domain-averaged relative humidity, $\overline{RH}$, due to evaporation during isobaric mixing can be obtained from $\overline{RH}(t)$ or $\overline{q_v}(t)$, the domain-averaged water vapor mixing ratio. RH is related to q_v:

$$RH = q_v / q_{v,s}(T, p).$$

During isobaric mixing and evaporation, $\overline{RH}$ approaches 1 while $\overline{q_v}$ approaches $\overline{q_{v,s}}$:

$$\frac{d(\overline{RH} - 1)}{dt} = \frac{d\overline{RH}}{dt} = -\frac{\overline{RH} - 1}{\tau_{RH}}. \tag{1}$$

Similarly,

$$\frac{d(\overline{q_v} - \overline{q_{v,s}})}{dt} \approx \frac{d\overline{q_v}}{dt} = -\frac{\overline{q_v} - \overline{q_{v,s}}}{\tau_{q_v}}. \tag{2}$$

When $d\overline{q_{v,s}}/dt = 0$, (1) can be obtained from (2) by dividing the latter by $\overline{q_{v,s}}$. During isobaric mixing, $d\overline{q_{v,s}}/dt \approx 0$. In this case, $\tau_{RH} = \tau_{q_v}$, so we may use $\overline{q_v}(t)$ alone to determine τ_{RH} using (2).

Our τ_{RH} is identical to *Jeffery and Reisner*'s [2006] τ_{efold}, Lehmann et al.'s τ_{react}, and to Kumar et al.'s τ_{relax}. As noted by Lehmann et al., this time scale is "related to the time required for phase changes associated with droplet evaporation and the restoration of saturation in the mixture."

2.2. τ_{phase}

The phase relaxation time scale characterizes how rapidly an equilibrium vapor saturation is reached by evaporation (or growth) of an entire population of droplets [*Jeffery and Reisner*, 2006; *Lehmann et al.*, 2009; *Kumar et al.*, 2013]. An expression to calculate the domain-averaged phase relaxation time scale following *Jeffery and Reisner* [2006, equation (3)] is

$$\tau_{phase} = \frac{1}{4\pi D_v \bar{N}} \frac{r + a}{r^2}, \tag{3}$$

where D_v is the (assumed constant) molecular diffusivity of water vapor, $\bar{N}$ is the domain-averaged droplet number concentration, r is the mean droplet radius, $a = 2$ μm is an accommodation length, and the small temperature dependence of τ_{phase} has been ignored. To apply (3) to mixing and evaporation after an entrainment event in the EMPM, we follow *Kumar et al.* [2013] and set $\bar{N} = \bar{N}(t_e)$ and $r = \bar{r}(t_e)$, where t_e is a time immediately following the entrainment event.

2.3. τ_{evap}

The droplet evaporation time scale, τ_{evap}, is the time scale for a single droplet to evaporate in subsaturated air [*Jarecka et al.*, 2013; *Kumar et al.*, 2013; *Lehmann et al.*, 2009]:

$$\tau_{evap} = \frac{r_v^2}{A(1-RH_e)}.$$ (4)

Here, r_v is the mean volume radius of the cloud droplets, RH_e is the relative humidity of the entrained air, and $A \approx 10^{-10}$ m^2 s^{-1}.

2.4. τ_σ

A time scale, τ_σ, for the decay of the domain-averaged standard deviation of water vapor, σ_{q_v}, due to mixing and evaporation can be defined similarly to τ_{RH}:

$$\frac{d\sigma_{q_v}}{dt} = -\frac{\sigma_{q_v}}{\tau_\sigma}.$$ (5)

2.5. τ_{eddy}

The eddy mixing time scale is

$$\tau_{eddy} \equiv \left(\frac{d^2}{\varepsilon}\right)^{1/3},$$ (6)

where d is the width of an entrained blob and ε is the dissipation rate of turbulent kinetic energy. It is a measure of the average time it takes for turbulent eddies to reduce the width of an entrained blob from d to the smallest eddy size.

2.6. τ_{sed}

Droplet sedimentation transports droplets into the entrained air. The time scale for sedimentation of droplets of radius r into a blob of entrained air of size d is

$$\tau_{sed} \equiv \frac{d}{V_t},$$ (7)

where $V_t = cr^2$ is the Stokes terminal velocity, and $c = 1.19 \times 10^8$ m^{-1} s^{-1}.

2.7. τ_{eddy}^*

Droplets fall through the air and can therefore fall into entrained air and evaporate. If there is no turbulence, a measure of the average time it takes for sedimentation to fill all of the entrained air with droplets is τ_{sed}. When there is droplet sedimentation and turbulent mixing, the two processes acting together allow the entrained air to evaporate droplets more quickly than if either process was acting alone. While droplets are falling into the entrained air, the average width of the entrained air filaments is simultaneously decreasing due to scale reduction by turbulent eddies. A generalized eddy mixing time scale that accounts for both droplet sedimentation and turbulent mixing is

$$\tau_{eddy}^* \equiv \frac{1}{\frac{1}{\tau_{eddy}} + \frac{1}{\tau_{sed}}},$$ (8)

where τ_{eddy} and τ_{sed} are defined by (6) and (7), respectively. The impact of sedimentation on droplet evaporation for a very slow mixing case may substantial. At more typical mixing rates, it is not.

2.8. Examples and Discussion

Two examples of what we believe actually occur during isobaric mixing and evaporation are shown in Figure 1. These results were obtained with the EMPM. Table 1 lists the mixing parameters and time scales for the two EMPM simulations and for one DNS performed by *Kumar et al.* [2013]. The time scales and Da for the DNS are similar to those for EMPM Case 1. It is not currently feasible to perform DNS for the high-Da regime of EMPM Case 2.

Comparison of the theoretical and actual time scales listed in Table 1 suggests that τ_{eddy}^* is a very good estimate of τ_σ, and that $\tau_{eddy}^* + \tau_{phase}$ and $\max(\tau_{eddy}^*, \tau_{phase})$ are good estimates of τ_{RH}. Results consistent with
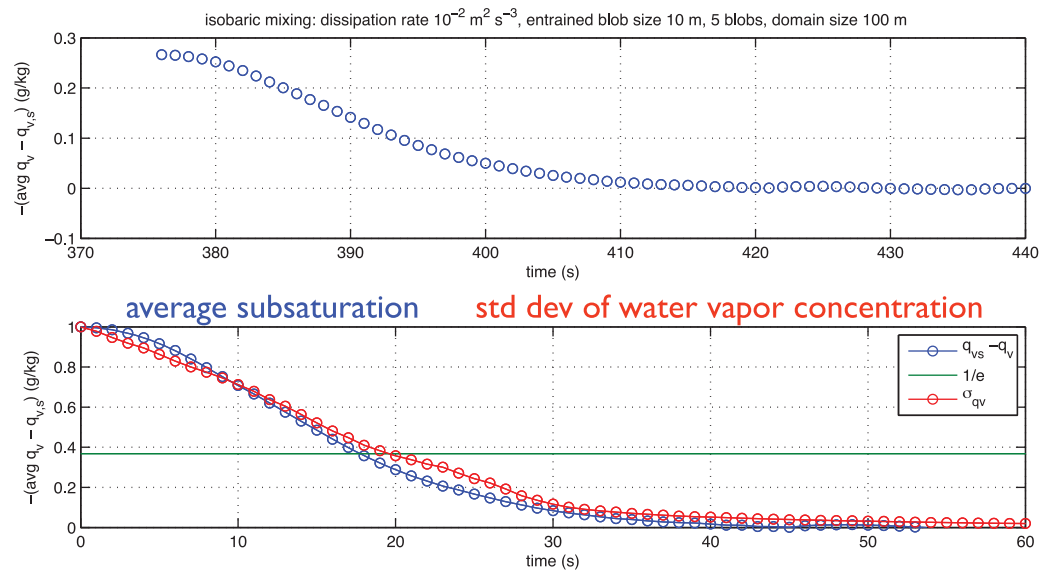
Figure 1. (top) Explicit Mixing Parcel Model simulation of isobaric mixing of saturated air (containing 100 cloud droplets per cm^3 of radius 15 μm) with one segment of subsaturated air 0.25 m in length in a 1-D domain 20 m in length, with a dissipation rate of 10^{-2} m^2 s^{-3}. The blue curve is the average subsaturation normalized by its initial value, the red curve is the standard deviation of the water vapor mixing ratio, and the green line is 1/e. The e-folding times for saturation adjustment and decay of water vapor standard deviation obtained from the plot are 5.5 and 1.2 s, respectively. The calculated evaporation and mixing time scales are 2.2 and 1.8 s, respectively.(bottom) Same as top plot except for mixing of five segments of subsaturated air (each 10 m in length) in a 1-D domain 100 m in length. The e-folding times for saturation adjustment and decay of water vapor standard deviation obtained from the plot are 18 and 20 s, respectively. The calculated evaporation and mixing time scales are 4 and 22 s, respectively.

the latter estimate were also obtained by *Jeffery and Reisner* [2006] and *Kumar et al.* [2013], and first hypothesized by *Magnussen and Hjertager* [1976].

Lehmann et al. [2009] calculated the time scales τ_{RH}, τ_{phase}, and τ_{evap} for monodisperse droplet populations in subsaturated air (i.e., already mixed so $\tau_{\text{eddy}} = 0$) and noticed that $\tau_{RH} = \min(\tau_{\text{phase}}, \tau_{\text{evap}})$ if either τ_{phase} or τ_{evap} is much smaller than the other, but that τ_{RH} can be much larger than τ_{phase} or τ_{evap} if they are approximately equal. In the DNSs performed by *Kumar et al.* [2013], Da based on the largest eddy time scale was at most 1.1 and the DNSs were thus dominated by homogeneous mixing. Kumar et al. found that $\tau_{RH} \approx \tau_{\text{phase}}$ in their DNSs, which were limited to cases for which $\tau_{\text{phase}} < \tau_{\text{evap}}$. In the 12 DNSs of Kumar et al. with

domain size 0.256 m, $\tau_{\text{eddy}} = 1.3$ s, which is less than the smallest value of τ_{phase} (2.3 s) in this set of simulations.

In the top plot of Figure 1, homogenization by mixing is rapid (i.e., $\tau_\sigma < \tau_{RH}$ and $\tau_{\text{eddy}}^* < \tau_{\text{phase}}$), so that adjustment to equilibrium (exact saturation in this isobaric scenario) occurs at the rate dictated by the droplet population properties (i.e., at the evaporation time scale) so that $\tau_{RH} \approx \tau_{\text{phase}}$.

In the bottom plot of Figure 1, homogenization by mixing and adjustment to exact saturation occur essentially simultaneously because the mixing time scale is

Table 1. Mixing Parameters and Time Scales for Two EMPM Simulations and One DNS Performed by *Kumar et al.* [2013][a]

Parameter	Case 1	Case 2	DNS
Domain size (m)	20	100	0.26
Entrained blob size (m)	0.25	10	0.17
Entrained air fraction	0.0125	0.50	0.67
Entrained air relative humidity	0.87	0.87	0.79
Dissipation rate (10^{-2} m^2 s^{-3})	1.00	1.00	0.34
Droplet number concentration (cm^{-3})	100	100	328
Droplet radius (μm)	15.65	15.65	15.00
τ_{eddy}	1.8	21.5	1.3
T_{sed}	8.6	343	∞
τ_{eddy}^*	1.5	20.3	1.3
τ_{phase}	2.2	4.2	3.1
τ_{evap}	18 .8	18.8	20.5
$\tau_{\text{eddy}}^* + \tau_{\text{phase}}$	3.7	24.5	4.4
τ_σ	1.2	20	
τ_{RH}	5.5	18	3.3
Da	0.8	5.1	0.4
l_* (m)	0.15	0.20	0.10

[a]The Damköhler number, Da, is $\tau_{\text{eddy}}/\tau_{\text{phase}}$ and the transition length scale, l_*, is $\epsilon^{1/2}\tau_{\text{phase}}^{3/2}$.
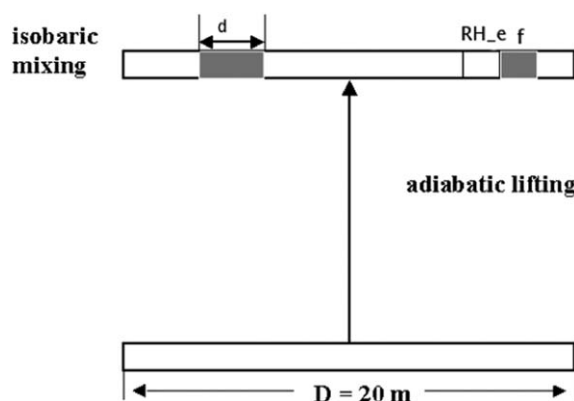
Figure 2. Schematic diagram of the model setup.

much larger than the phase relaxation time scale (i.e., $\tau^*_{\text{eddy}} \gg \tau_{\text{phase}}$), and therefore limits (and determines) the grid-averaged evaporation rate, so that $\tau_{RH} \approx \tau^*_{\text{eddy}}$. This scenario is typical of mixing in cumulus clouds.

3. Model Description and Simulation Parameters

The EMPM predicts the evolving in-cloud variability of temperature and water vapor due to entrainment and finite-rate turbulent mixing using a one-dimensional (1-D) representation of a rising cloudy parcel. The 1-D formulation allows the model to resolve fine-scale variability down to the smallest turbulence scales (about 1 mm). In all simulations, the domain size is 20 m (x) × 1 mm (y) × 1 mm (z) with 12,000 grid cells. The EMPM calculates the growth of thousands of individual cloud droplets based on each droplet's local environment. To characterize the evolution of the DSD due to isobaric entrainment and mixing events for a range of conditions, the following sequence of events was simulated, as illustrated in Figure 2. Initially a parcel of cloudy air ascends adiabatically above cloud base. At 750 m above cloud base, the parcel entrains one or more blobs (segments) of environmental air followed by isobaric mixing until homogenization. Each segment of subsaturated entrained air replaces a segment of the cloudy parcel of the same size and the cloudy and newly entrained air undergoes a finite-rate turbulent mixing process. Droplets grow or evaporate depending on their local microphysical environments which they encounter during this process. The EMPM results include the droplet radius and saturation ratio histories. For the purposes of this paper, two realizations of each simulation case were run.

Figure 2 illustrates the design of our EMPM simulations. The EMPM domain adiabatically ascends from 964 hPa, which is just below cloud base, to 883 hPa, where one entrainment event occurs, except for one set of cases in which multiple entrainment events occur. Figure 2 also shows schematically the entrainment and mixing parameters that were varied in the simulations; see also Table 2. Analyses are performed on three sets of simulations with a range of entrained environmental air fractions (f): (1) for the environmental relative humidity (RH_e) of the entrained segment, (2) for the turbulent dissipation rate (ϵ), and (3) for the size of the entrained blob of environmental air (d). The DSDs of these sets are compared to a control case to isolate the DSD changes due to entrainment and mixing. The parameters for the control case ($RH_e = 87.4\%$, $\epsilon = 10^{-2}$ m^2 s^{-3} and $d = 2$ m) have typical values measured for a cumulus cloud. Single versus multiple entrainment events were also considered. The initial conditions at cloud base were taken from the Hawaiian observations of *Raga et al.* [1990]; see Table 2. For each case, two simulations were performed, each with a different random number seed. More than 70 cases—with two realizations each—of entrainment and isobaric mixing were performed and analyzed that cover a wide range of entrainment scenarios. Table 3 lists the eddy mixing time scale, τ_{eddy}, of the various EMPM simulations, while Table 4 presents the dependence of the phase relaxation time scale, τ_{phase}, of the EMPM simulations on the entrainment fraction, f. The former range from about 5 s to more than 100 s, while the latter range from about 6 s for $f = 0.1$ to about 18 s for $f = 0.7$. For $f = 0.1 – 0.3$ for the control case and reduced

Table 2. Parameters for the EMPM Simulations of DSD Evolution After Entrainment and Isobaric Mixing

Parameter	Value
Cloud base conditions	
Droplets concentration N_d	102.75 cm^{-3}
Pressure p_b	963.95 hPa
Temperature T_b	293.56 K
Water vapor mixing ratio q_{vb}	15.73 g kg^{-1}
Vertical velocity w	2 m s^{-1}
Domain size D	20 m
Entrainment parameters	
Pressure p_e	883.28 hPa
Blob size d	1, 2 (control), 4, 6, 10 m
Entrainment fraction f	0.1–0.9
Relative humidity RH_e	0.87 (control),
of entrained air	0.44, 0.22
Turbulence dissipation rate ε	10^{-2} (control), 5×10^{-3}, 10^{-4}, 10^{-6} m^2 s^{-3}

Table 3. Eddy Mixing Time Scale, τ_{eddy}, of the Various EMPM Simulations

Case	τ_{eddy} [s]
Control with $d = 2$ m, $\epsilon = 10^{-2}$ m² s⁻³	
	7.4
Different entrained blob sizes with $\epsilon = 10^{-2}$ m² s⁻³	
$d = 1$ m	4.6
$d = 2$ m	7.4
$d = 4$ m	12
$d = 6$ m	15
$d = 10$ m	22
Different entrained blob sizes with $\epsilon = 10^{-4}$ m² s⁻³	
$d = 2$ m	34
$d = 4$ m	54
$d = 6$ m	71
$d = 10$ m	100
Different dissipation rates with $d = 2$ m	
$\epsilon = 10^{-2}$ m² s⁻³	7.4
$\epsilon = 5 \times 10^{-3}$ m² s⁻³	9.3
$\epsilon = 10^{-4}$ m² s⁻³	34
$\epsilon = 10^{-6}$ m² s⁻³	160
Different humidities with $d = 2$ m, $\epsilon = 10^{-2}$ m² s⁻³	
$RH_e = 0.87$	7.4
$RH_e = 0.44$	7.4
$RH_e = 0.22$	7.4

humidity cases (for which $d = 2$ m and $\epsilon = 10^{-2}$ m²s⁻³), $\tau_{\text{eddy}} \leq \tau_{\text{phase}}$. In these rapid mixing cases, adjustment to equilibrium occurs at the rate dictated by the evaporation time scale, τ_{phase}. For all other cases with $f = 0.1 – 0.3$, and for most other cases with $f = 0.4 – 0.7$, the mixing time scale is larger than the evaporation time scale, and therefore limits (and determines) the grid-averaged evaporation rate.

4. Bulk Microphysical Changes Due to Isobaric Mixing of Entrained Air

During mixing, droplets evaporate until either the parcel is uniformly saturated with droplets present, or uniformly subsaturated with no droplets present. The amount of liquid water that evaporates is determined entirely by the thermodynamic properties of the parcel before entrainment, of the temperature and relative humidity (RH_e) of the entrained air, and of the entrainment fraction (f), or equivalently, by the mean thermodynamic properties of the parcel immediately after entrainment. It can be shown that the change in the average liquid water mixing ratio ($\overline{q_c}$) during isobaric mixing is

$$\Delta \overline{q_c} \approx f(1 - RH_e)(\overline{q_v^*})_i,$$

where $(\overline{q_v^*})_i$ is the average saturation mixing ratio of the cloudy parcel before entrainment and mixing. The relationship is exact only if the temperature of the parcel does not change due to entrainment, mixing, and evaporation. The *fraction* of $(\overline{q_c})_e$ that evaporates during mixing is

$$\frac{(\overline{q_c})_m}{(\overline{q_c})_e} = \frac{f}{1-f}(1 - RH_e)\frac{(\overline{q_v^*})_i}{(\overline{q_c})_i},$$

where $(\overline{q_c})_i$, $(\overline{q_c})_e$, and $(\overline{q_c})_m$ are the average liquid water mixing ratios before entrainment, just after entrainment, and after mixing. For all of our cases, $(\overline{q_v^*})_i / (\overline{q_c})_i \approx 2.6$.

The fraction of $(\overline{q_c})_i$ that remains after dilution by entrainment is simply $1 - f$. Therefore, the fraction of $(\overline{q_c})_i$ that remains after entrainment, mixing, and evaporation is

$$\frac{(\overline{q_c})_m}{(\overline{q_c})_i} \approx (1-f)\left(1 - \frac{(\overline{q_c})_m}{(\overline{q_c})_e}\right) = (1-f) - f(1 - RH_e)\frac{(\overline{q_v^*})_i}{(\overline{q_c})_i}. \tag{9}$$

Table 4. The Dependence of the Phase Relaxation Time Scale, τ_{phase}, of the EMPM Simulations on the Entrainment Fraction, f

f	τ_{phase} [s]
0.1	5.9
0.2	6.6
0.3	7.5
0.4	8.8
0.5	10.5
0.6	13.0
0.7	17.6

A single-moment bulk microphysics parameterization applied to our isobaric entrainment and mixing scenario would predict $(\overline{q_c})_m$ using essentially (9). A second-moment bulk scheme would also attempt to predict N_m, the cloud droplet number concentration after entrainment, mixing, and evaporation. Whereas $(\overline{q_c})_m$ is completely determined by the bulk properties of the parcel and the entrained air, N_m depends, in addition, on the details of the mixing process.

Because $\overline{q_c} = (\rho_w / \rho) N V$, where ρ_w is the density of liquid water, ρ is the density of dry air, and $V \equiv (4\pi/3)r_v^3$ is the mean droplet volume, we can write
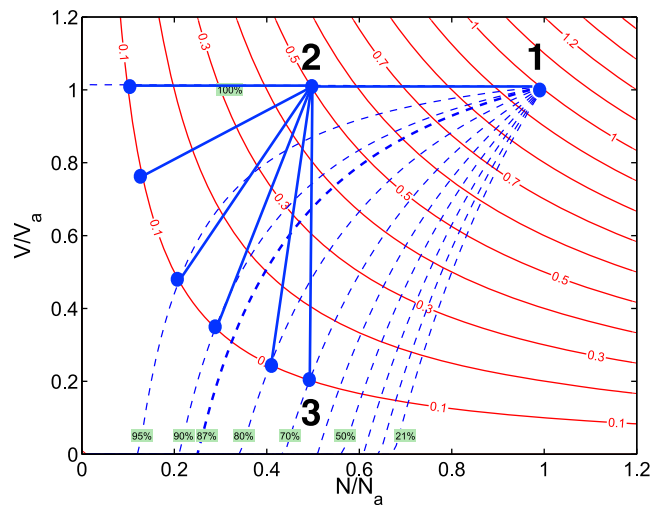
Figure 3. Example N-V diagram. The red lines are the isolines of the LWC dilution ratio given by (9). The blue dashed lines are described in the text. Point 1 indicates the parcel properties before entrainment. Point 2 indicates the parcel properties after entrainment but before mixing. Point 3 indicates the parcel properties after mixing and droplet evaporation have uniformly saturated the parcel without completely evaporating any droplets. The remaining, unlabeled, points represent scenarios in which some of the droplets completely evaporate, thereby reducing N.

$$\frac{\overline{q_c}}{(\overline{q_c})_i} = \frac{N}{N_i}\frac{V}{V_i}, \qquad (10)$$

where each subscript i indicates an initial value. In our case, these will be the adiabatic values just before entrainment.

When entrainment occurs, N is reduced by dilution from N_i to $N_e = (1-f)N_i$. During mixing and evaporation, N may be further reduced if some droplets completely evaporate. If none of the droplets completely evaporate during mixing, then $N_m = N_e = (1-f)N_i$. Even if the entrained air contains CCN, the CCN will usually not become activated without further ascent.

A diagram with x and y coordinates N/N_i and V/V_i, respectively, is called an N-V or mixing diagram [*Burnet and Brenguier*, 2007; *Gerber et al.*, 2008; *Lehmann et al.*, 2009; *Lu et al.*, 2013]. Contours of $\overline{q_c}/(\overline{q_c})_i$ based on (10) are usually added. Such a diagram is a convenient way to graphically represent N, V, and LWC for different mixing scenarios. Figure 3 is an example. Point 1 on the diagram indicates the values before entrainment. Point 2 indicates the values just after entrainment. Point 3 indicates the values after droplet evaporation has uniformly saturated the parcel, but without completely evaporating any droplets, so $N_m = N_e$. (This is "homogeneous mixing" as defined in the introduction.) The remaining, unlabeled, points represent scenarios in which some of the droplets completely evaporate, thereby reducing N so that $N_m < N_e$ ("inhomogeneous mixing"). The greatest reduction of N is achieved by completely evaporating 90% of the droplets, while the other 10% do not evaporate at all ("extreme inhomogeneous mixing"). In this case, the droplet population retains its initial mean volume radius.
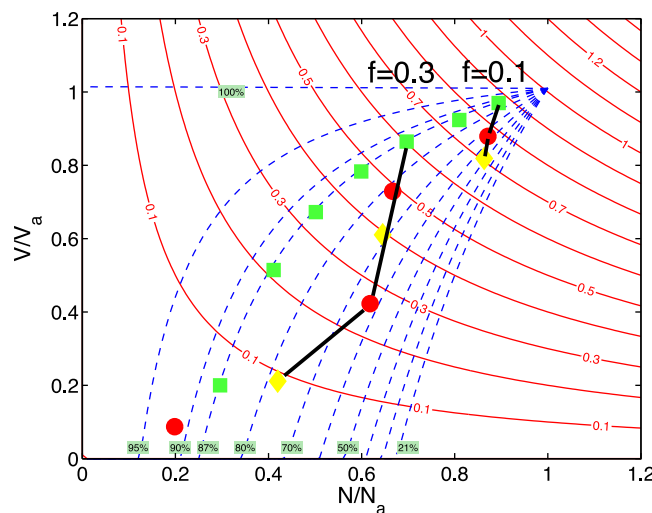

Figure 4. N-V diagram for $RH_e = 0.87$ and $f = 0.1, 0.3, 0.5,$ and 0.7 (green squares), $RH_e = 0.44$ and $f = 0.1, 0.2, 0.3,$ and 0.4 (red circles), and $RH_e = 0.22$ and $f = 0.1, 0.2,$ and 0.3 (yellow diamonds), all with $d = 2$ m and $\epsilon = 10^{-2}$ m^2 s^{-3}. The red lines are the isolines of the LWC dilution ratio given by (9). The blue dashed lines are described in the text.

Because the parcel's LWC after entrainment and mixing is determined entirely by the bulk properties of the parcel and the entrained air, point 3 and the five unlabeled points all have the same LWC. The value of the LWC is determined by (9), which depends only on the entrained air's fraction and its relative humidity, and the factor $(\overline{q_v^*})_i/(\overline{q_c})_i$ which depends only on the cloud base properties and the entrainment level. When no cloud droplets completely evaporate during mixing, $N_m/N_i = (1-f)$, so that f and RH_e completely determine N, V, and LWC. Each dashed blue line in Figure 3 depicts N, V, and LWC
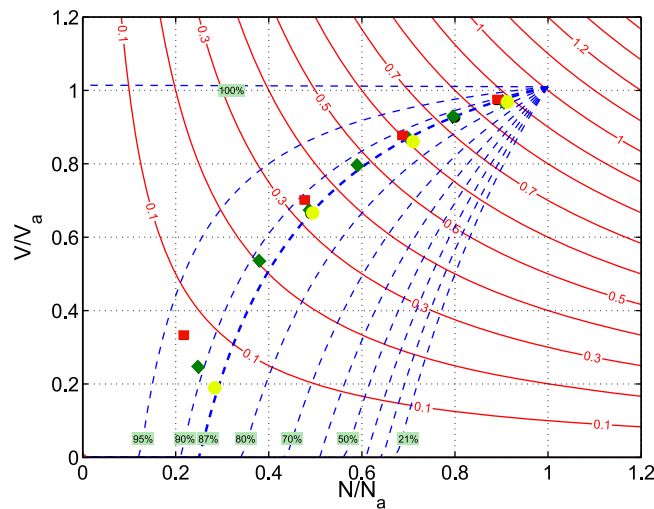
Figure 5. N-V diagram for $\epsilon = 5 \times 10^{-3}$ m^2 s^{-3} and $f = 0.1, 0.2, 0.3, 0.5,$ and 0.7 (yellow circles), $\epsilon = 10^{-4}$ m^2 s^{-3} for $f = 0.1, 0.2, 0.3, 0.5, 0.6,$ and 0.7 (green diamonds), and $\epsilon = 10^{-6}$ m^2 s^{-3} for $f = 0.1, 0.3, 0.5,$ and 0.7 (red squares), all with $d = 2$ m and $RH_e = 0.87$. The red lines are the isolines of the LWC dilution ratio given by (9). The blue dashed lines are described in the text.

versus $1 - f$ for the indicated value of RH_e for this mixing scenario. We emphasize that the only constraint on the scenarios that the dashed blue lines portray is that no droplets completely evaporate during entrainment and mixing. We will show in detail that these constraints on this mixing scenario do not restrict nor determine the degree of broadening that initially narrow adiabatic DSDs experience.

Figure 4 displays the parcel properties calculated by the EMPM after entrainment and mixing for $RH_e = 0.87, 0.44,$ and 0.22, for several entrainment fractions each, and with $d = 2$ m and $\epsilon = 10^{-2}$ m^{2}s^{-3}. Each point lies upon the heavy dashed blue line labeled with the RH_e for that case unless some of the droplets completely evaporated during mixing. For $RH_e = 0.87$, all of the points lie on the no-complete-evaporation (NCE) line, but this is not the case for the $RH_e = 0.44$ and 0.22 points, which exhibit significant departures from their NCE lines. Two sets of points, one for $f = 0.1$ and the other for $f = 0.3$, for all three RH_e values are indicated on Figure 4. If none of the droplets completely evaporated for any RH_e, the points would form a vertical line with $N_m = N_e = (1-f)N_i$. For $RH_e = 0.22$ and $f = 0.3$, complete droplet evaporation reduces N by as much as dilution by entrainment does. For all of these cases, the eddy mixing time scale, τ_{eddy}, is the same. The fraction of droplets that completely evaporates increases with both the entrained air fraction, f, and the subsaturation of the entrained air, $1 - RH_e$.

Figure 5 displays the parcel properties calculated by the EMPM after entrainment and mixing for three dissipation rates, with $RH_e = 0.87$ and $d = 2$ m. For these cases, τ_{eddy} increases as the dissipation rate decreases, as shown in Table 3. The fraction of droplets that completely evaporates increases with both f and τ_{eddy}.
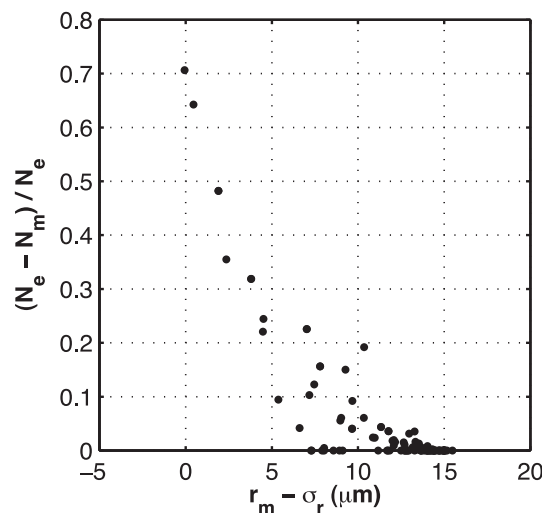

Figure 6. $r_m - \sigma_r$, a measure of the extension of the DSD toward zero radius versus $(N_e - N_m)/N_e$, the fraction of droplets that completely evaporated during mixing, for all cases with $N_m > 0$.

These results can be understood by considering how the DSD evolves due to mixing and evaporation. The DSD can be characterized by the mean droplet radius, r_m, and the standard deviation of the droplet radius, σ_r. Just before completely evaporating, a droplet's radius must be close to zero. This implies that the DSD includes some droplet radii near zero, which suggests that $r_m - \sigma_r$ may be a useful measure of the fraction of droplets that completely evaporate. Figure 6 confirms this.

Bulk double-moment microphysics schemes need to parameterize the change, if any, in droplet number concentration due to complete evaporation during mixing. *Jarecka et al.* [2013] presented a method that allows local prediction of the subgrid-scale mixing scenario by merging a double-moment microphysics scheme with an approach that represents the effects of turbulent entrainment and mixing proposed by *Grabowski* [2007] and further refined in *Jarecka et al.* [2009].
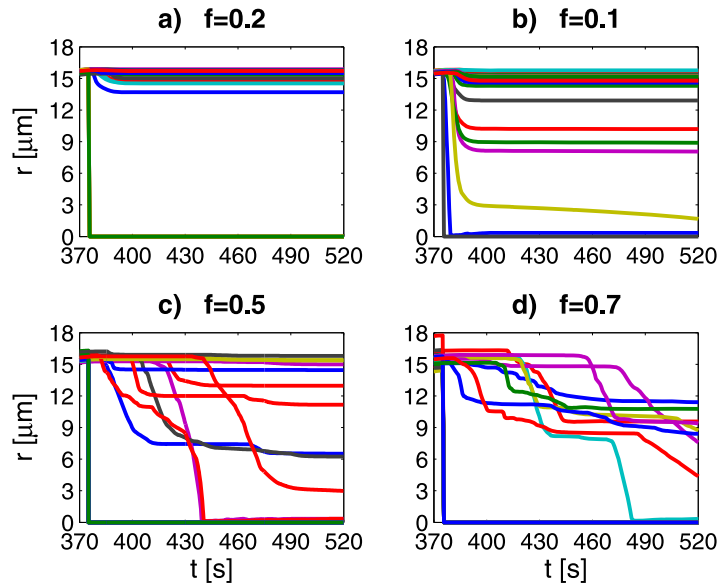
Figure 7. A 30 droplet radius histories (different colors) from just before entrainment at 375 s until mixing is completed for (a) the control case, (b) the reduced humidity case ($RH_e = 0.22$), (c) the larger entrained blob case ($d = 10$ m) with $\epsilon = 10^{-4}$ m^2 s^{-3}, and (d) the slower mixing case ($\epsilon = 10^{-6}$ m^2 s^{-3}).

Jarecka et al.'s method uses a parameterization suggested by *Andrejczuk et al.* [2006] that is based on the ratio of the mixing time scale τ_{eddy} and the droplet evaporation time scale, τ_{evap}. Figure 6 suggests that a different method for determining changes in *N* during mixing may be feasible if one can determine how r_m and σ_r evolve during mixing. Further investigation of parameterizing the change in *N* due to mixing will be left to a future study.

The DSD is important not only for determining changes in *N* during mixing, but also for its influence on the growth of droplets by collision and coalescence, which is our primary motivation for studying how the DSD is affected by entrainment and mixing.

5. Simulated Effects of Entrainment and Mixing on the Droplet Size Distribution

An overview of the radius histories of 30 droplets is given in Figure 7 from just before entrainment until mixing is completed for four different experiments (the control case, the reduced humidity case ($RH_e = 0.22$), the larger blob size case ($d = 10$ m) and the slower mixing case ($\epsilon = 10^{-6}$ m^2 s^{-3}). Each case has a different droplet radius evolution, which lead to diverse DSDs. For the larger entrained blob size and slower mixing cases, the reduction in the radius shows multiple steps. Most droplets evaporate by small amounts whereas a few decrease their radii enormously and multiple times.

In the following sections, we describe how DSDs are affected by entrainment and isobaric mixing for a wide range of entrained air properties (entrained air fraction, entrained blob size, and relative humidity), and turbulence intensities.

5.1. Measures of DSD Broadening
When the solution and curvature effects are neglected, droplet growth due to condensation or evaporation can be approximated by

$$r\frac{dr}{dt} = S\xi, \tag{11}$$

where r is droplet radius, S is the supersaturation, and ξ is the normalized condensation growth parameter, which is a function of temperature and pressure [*Rogers and Yau*, 1989]. If (11) is integrated from time t_1 to time t_2, and the droplet growth or evaporation occurs at approximately constant temperature and pressure, we obtain

$$\Delta r^2 \equiv r^2(t_2) - r^2(t_1) = \xi\int_{t_1}^{t_2} S\,dt. \tag{12}$$

Thus, the change in a droplet's radius squared is determined by the droplet's saturation history, $\mathcal{S} \equiv \int_{t_1}^{t_2} S\,dt$, and the evolution of a droplet size distribution (DSD) is governed by the distribution of $\mathcal{S}$. We will characterize the distribution of $\mathcal{S}$ by the standard deviation of Δr^2, $\sigma_{\Delta r^2}$. A commonly used measure of DSD width is
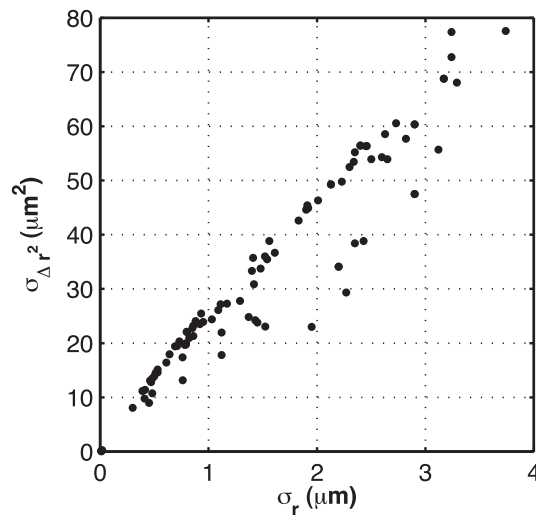
Figure 8. The standard deviation of the radius, σ_r, versus the standard deviation of the change in the radius squared, $\sigma_{\Delta r^2}$, after entrainment and isobaric mixing, for all single entrainment event cases.

the standard deviation of the droplet radius, σ_r. These two measures are compared in Figure 8 which shows that they are approximately linearly related, but not uniquely so.

5.2. Control Case Versus Instant Mixing Case

Instant mixing occurs when the eddy mixing time scale becomes very small, which occurs when the entrained blob size d becomes very small, or the turbulence dissipation rate becomes very large. Parcel models that do not represent internal structure implicitly assume instant mixing. The calculated DSDs after entrainment and mixing for instant mixing compared to the control case after mixing is completed for the full range of f values ($f = 0.1$–0.9) are shown in Figure 9. Only one radius mode is obtained for both cases. In both cases, a few very small droplets are left over for the highest entrainment fraction. For the control case the droplet spectra are broadened after entrainment and mixing. For higher entrained air fractions the peak (highest concentration radius) is decreased in magnitude and is shifted toward smaller radius sizes. The DSDs of the instant mixing cases shift to smaller droplet radii with increasing entrained air fractions leaving the width of the distributions unchanged. The droplets evaporate uniformly in these cases with no variation in the supersaturation in space.
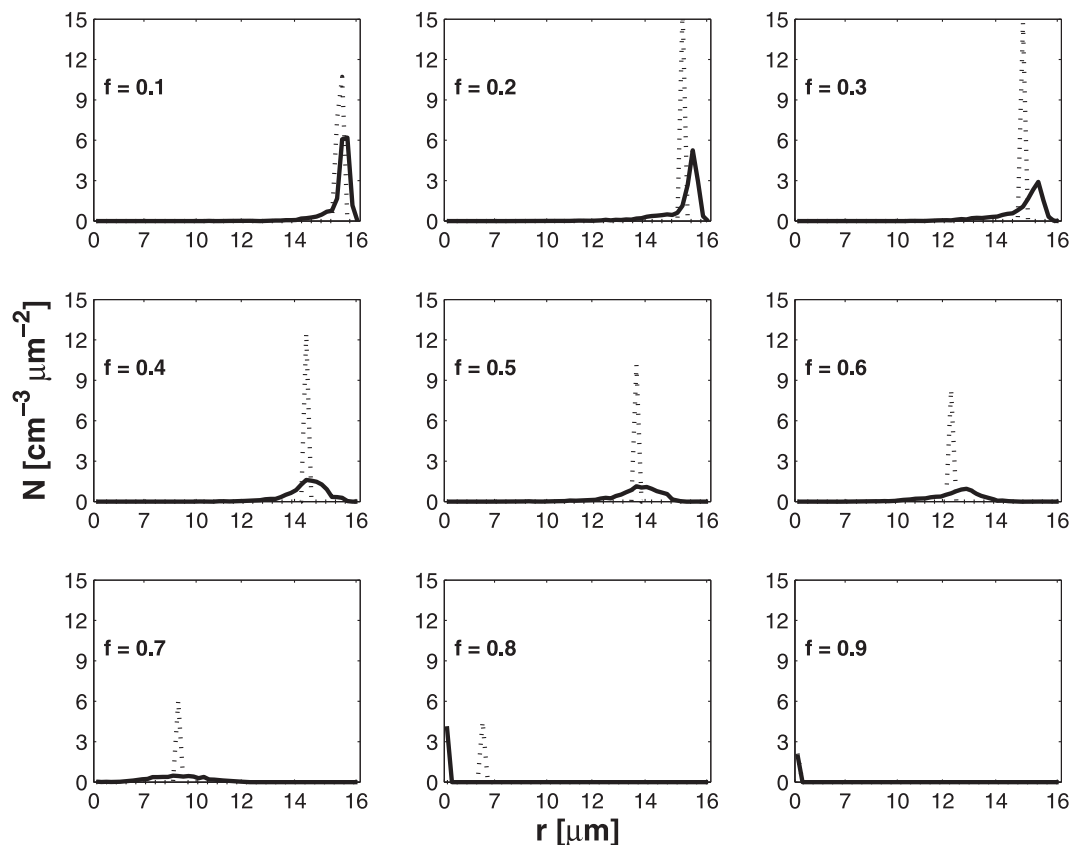

Figure 9. Droplet spectra for the control (solid) versus instant mixing (dotted) case with entrainment fractions $f = 0.1$–0.9.
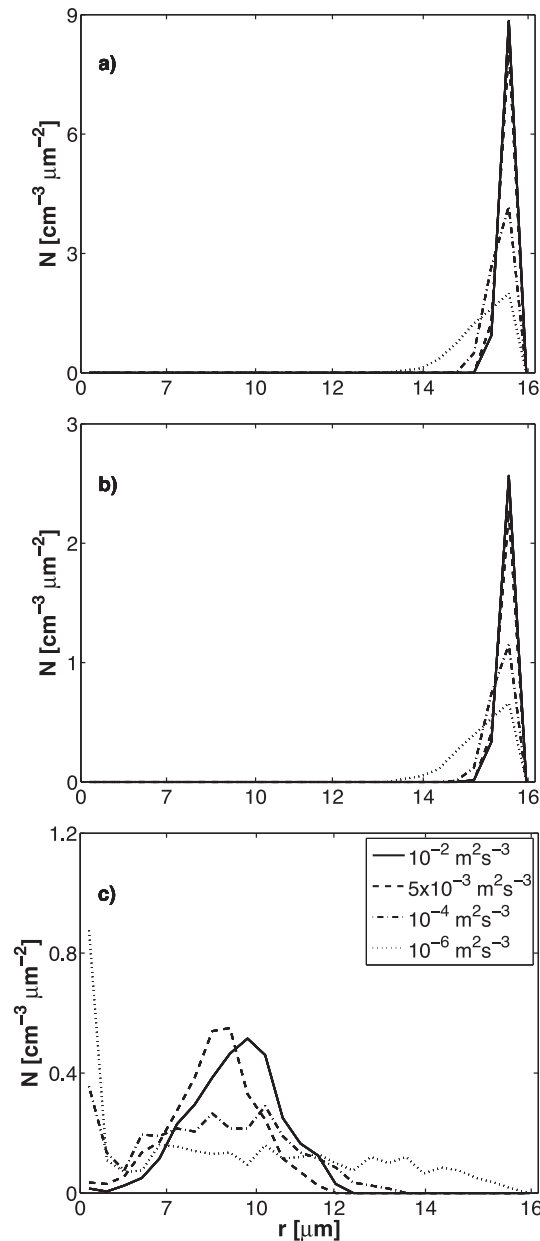
Figure 10. Droplet spectra for entrained air fraction $f = 0.7$ and $RH_e = 0.87$ for different dissipation rates $\epsilon = 10^{-2}$ (solid), 5×10^{-3} (dotted), 10^{-4} (dashed dotted), 10^{-6} (dashed) m^2 s^{-3} (a) just before entrainment, (b) just after entrainment, and (c) after mixing is completed.

One idealization of the mixing and evaporation process between cloudy and clear air, denoted "homogeneous mixing," is that the homogenization is instantaneous, in which case all of the cloud droplets experience the same subsaturation and consequently evaporate equally, which leads to the narrow DSDs shown in Figure 9 for instant mixing (dotted lines). It is evident that this idealization is not consistent with more physically realistic, finite-rate mixing of the control case shown in Figure 9 (solid lines).

5.3. Control Case Versus Reduced Dissipation Rates

Figure 10 shows the DSDs for different dissipation rates for entrainment fraction $f = 0.7$. Note that $\epsilon = 10^{-2}$ m^2 s^{-3} is the control case. Figure 10a represents the DSDs just before entrainment, Figure 10b just after entrainment, and Figure 10c after mixing is completed. Mixing broadens all of the DSDs, especially for the two slowest mixing cases as shown in Figure 10c. Note that for the slowest mixing case, the droplets from about 2 to 15 μm are almost uniformly distributed over all radius size categories.

The reason for the differences is evident in Figure 11, which shows the average radius (r_{ave}) and the supersaturation histories for four droplets for $\epsilon = 10^{-4}$ m^2 s^{-3} (top) and $\epsilon = 10^{-6}$ m^2 s^{-3} (bottom). Some of the droplets encounter regions of subsaturated air at later times for $\epsilon = 10^{-6}$ m^2 s^{-3} because the mixing takes longer. Droplets grow or evaporate according to their different local environments, some of which remain subsaturated for longer periods of time with slower mixing. As a result, their saturation histories are more variable.

Figure 12 presents droplet spectral width (σ_{dr^2}) for the control case and for different dissipation rates. It shows that high turbulence levels lead to lower σ_{dr^2}, low turbulence levels give significantly wider droplet spectra, and for all dissipation rates, σ_{dr^2} increases with the degree of dryness, $f(1-RH_e)/(1-f)$.
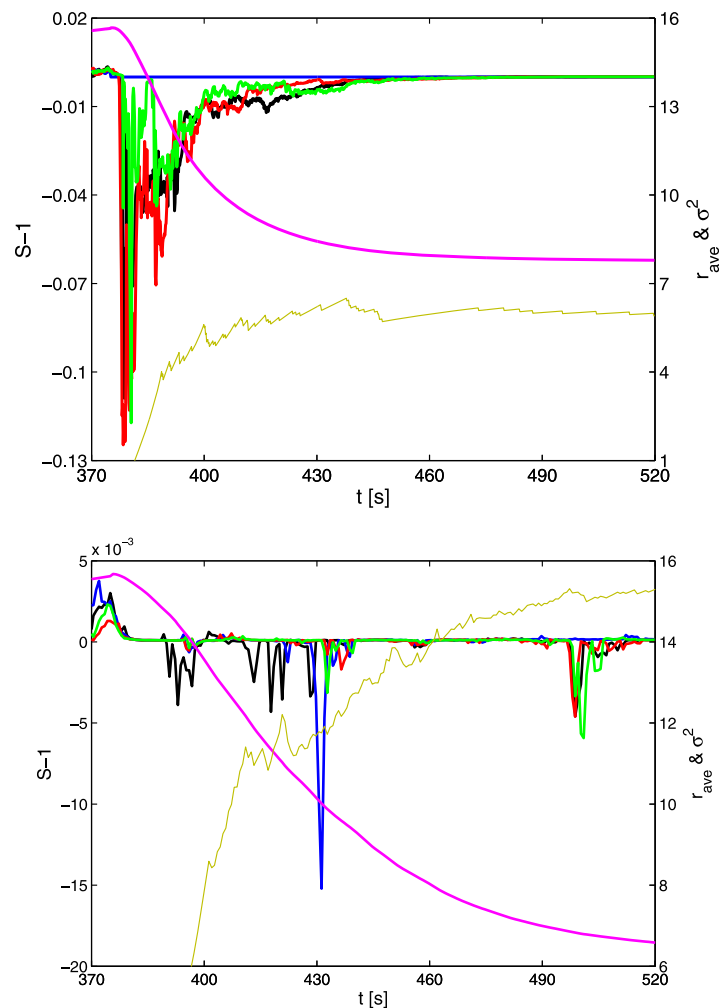
5.4. Control Case Versus Different Blob Sizes

Smaller and larger blobs than for the control case are entrained in this set. The eddy mixing time scale increases with the entrained blob size (Table 3). For smaller blobs, the blob size was reduced to half of its original size ($d = 1$ m) but the entrainment fraction was kept constant. For the larger blobs only one blob ($d = 4, 6, 10$ m) was entrained with respect to entrainment fractions $f = 0.2, 0.3, 0.5$. Note that the dissipation rate for one experiment with the larger entrained blob is lower ($\epsilon = 10^{-4}$ m^2 s^{-3}) than that for the control case (Table 3).

Figure 13 shows the DSD results for the different entrained blob sizes compared to the control case for various entrainment fractions. The spectra for smaller blob sizes (dotted) are narrower compared to the control

Figure 11. Average radius (r_{ave}) for all r > 0.1 μm (magenta) with their variance σ^2 (yellow) and S-1 history (black, blue, red, green) of four droplets for (top) $\epsilon = 10^{-4}$ m^2 s^{-3} and (bottom) $\epsilon = 10^{-6}$ m^2 s^{-3} for f = 0.7 and RH_e = 0.87.
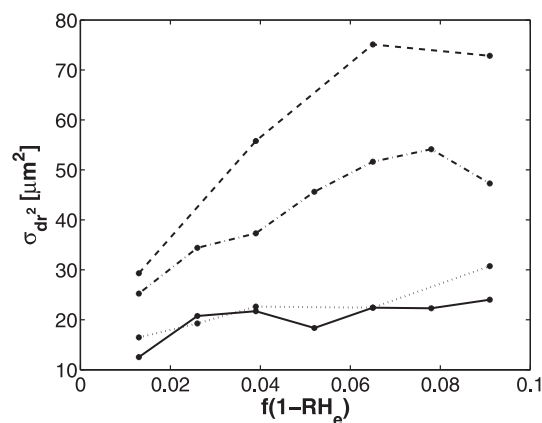

Figure 12. Droplet spectral width σ_{dr^2} for the control case and for different dissipation rates, all with RH_e = 0.87: $\epsilon = 10^{-2}$ m^2 s^{-3} (control, solid), $\epsilon = 5 \times 10^{-3}$ m^2 s^{-3} (dotted), $\epsilon = 10^{-4}$ m^2 s^{-3} (dashed dotted), and $\epsilon = 10^{-6}$ m^2 s^{-3} (dashed) as a function of $f(1 - RH_e)$.

case. Smaller entrained blobs have a narrower DSD due to the rapid break down of the smaller entrained eddies which is comparable to the large ϵ case. The greatest differences are found for the f = 0.5 cases. For larger entrained blob sizes and for f = 0.5 with $\epsilon = 10^{-4}$ m^2 s^{-3}, the spectrum broadens more to larger droplet sizes and less to smaller droplet sizes compared to the control case. For one entrained large blob it takes longer to mix. Therefore, not so many droplets are affected by the subsaturated air which is similar to the small ϵ case. For larger entrained blobs with $\epsilon = 10^{-2}$ m^2 s^{-3} this broadening feature is less pronounced.

Figure 14 shows the calculated droplet spectrum widths (σ_{dr^2}) as a function of degree of dryness for different blob sizes. Larger or smaller entrained blob sizes with $\epsilon = 10^{-2}$ m^2 s^{-3} up to an entrained fraction of 0.3 do not contribute much to an increase in the spectral width.

5.5. Control Case Versus Reduced Humidity Cases

Figure 15 shows the DSDs after mixing is completed for the reduced environmental humidity experiment compared to the control case for entrainment fractions f = 0.1–0.4. For a given entrained air fraction, the largest spectral width is obtained with the driest air entrained. The peak of the DSD with the driest entrained air is decreased most and shifted toward smaller radius sizes. Drier entrained air requires more evaporation and—for this eddy mixing time scale (7.4 s)—complete evaporation of some droplets to regain saturation, and therefore the DSDs are broadened and shifted toward smaller sizes as the entrained air fraction and RH_e decreases.

To examine how the droplet spectra depend on the degree of dryness, $f(1-RH_e)/(1-f)$, (a measure of how much LWC must be evaporated to saturate the mixed parcel), we show σ_{dr^2}, the standard deviation of Δr^2, the change
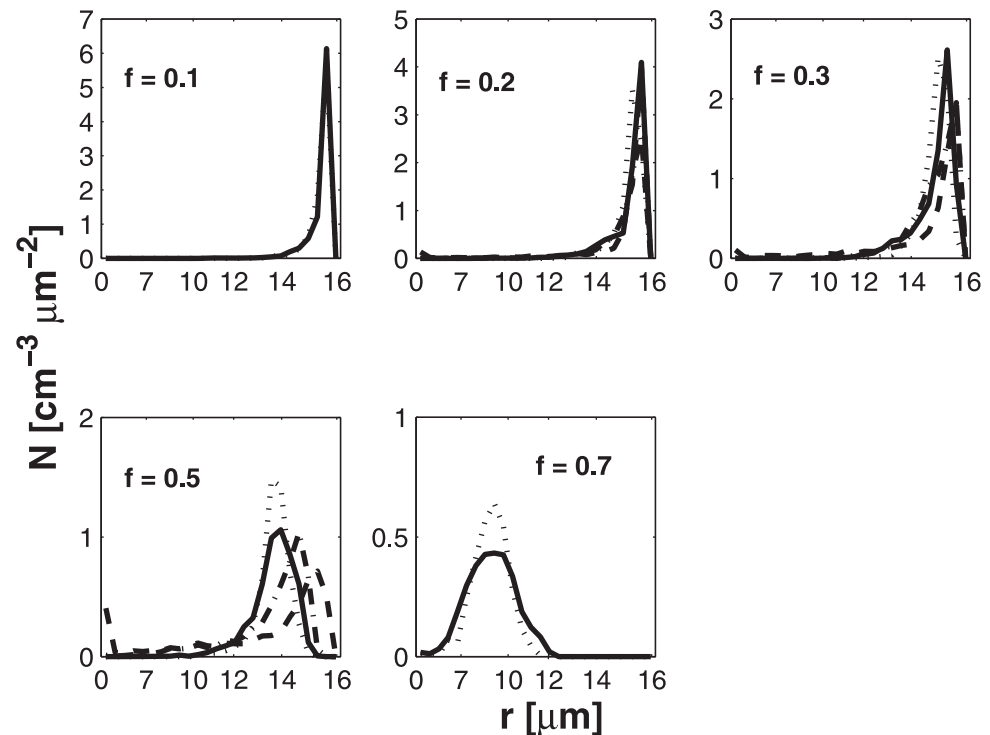
Figure 13. DSD for different entrained blob sizes: smaller blobs (dotted) and control (solid) with entrainment fractions $f = 0.1, 0.2, 0.3, 0.5, 0.7$; larger blobs ($d = 4, 6,$ and 10 m, dashed dotted) for $\epsilon = 10^{-2}$ m^2 s^{-3} and larger blobs ($d = 4, 6,$ and 10 m, dashed) for $\epsilon = 10^{-4}$ m^2 s^{-3} with respect to entrainment fractions $f = 0.2, 0.3, 0.5$ and $RH_e = 0.87$.

of droplet radius squared, due to isobaric mixing, as a function of $f(1-RH_e)/(1-f)$ for the various cases. For reference, σ_{dr^2} for a uniform DSD between radii of 0 and 15.65 μm is 81.6 μm^2. Figure 16 presents σ_{dr^2} for two realizations averaged for the reduced humidity cases compared to the control case. For the control case, σ_{dr^2} is relatively small. However, σ_{dr^2} is much larger for both of the drier entrained air cases. At a degree of dryness greater than about 0.2, σ_{dr^2} no longer increases because *all* droplets decrease in radius and none remain unaffected by evaporation as shown in Figure 15
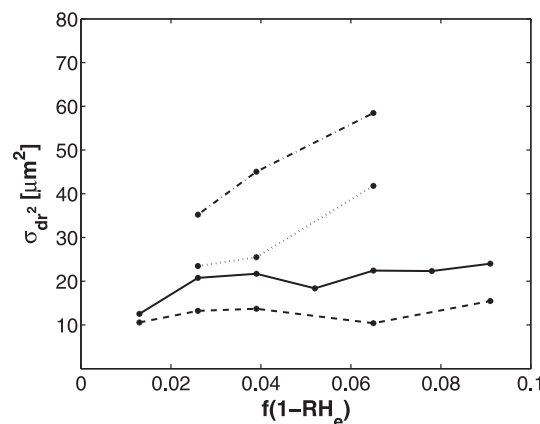

Figure 14. Droplet spectral width σ_{dr^2} for the control case and for different entrained blob sizes, all with $RH_e = 0.87$: $d = 1$ m (dashed), $d = 2$ m (control, solid), larger blob sizes ($d = 4, 6, 10$ m for $f = 0.2, 0.3, 0.6$) with $\epsilon = 10^{-2}$ m^2 s^{-3} (dotted) and $\epsilon = 10^{-4}$ m^2 s^{-3} (dashed dotted) as a function of $f(1-RH_e)$.

5.6. DSD Broadening

In this section, we have presented the dependence of DSD broadening due to entrainment and isobaric mixing on turbulence dissipation rate, entrained blob size, entrained air relative humidity, and entrained air fraction for given initial values of droplet radius and droplet number concentration. As shown in sections 2 and 4, the parameters ϵ and d determine the eddy mixing time scale, τ_{eddy}, while the parameters f and RH_e determine the change in LWC due to entrainment and mixing. Figure 17 incorporates results from all of the $RH_e = 87\%$ cases, which include all of the cases listed in Table 3 except those for $RH_e = 44\%$ and 22%, and indicates that for *this* RH_e the DSD width, σ_r, is determined by τ_{eddy} and the change in LWC due to entrainment and mixing. However, for $RH_e = 44\%$ and 22%, σ_r is several times larger for the same values of LWC and τ_{eddy}, as shown in Figure 18. This result indicates that fully quantifying
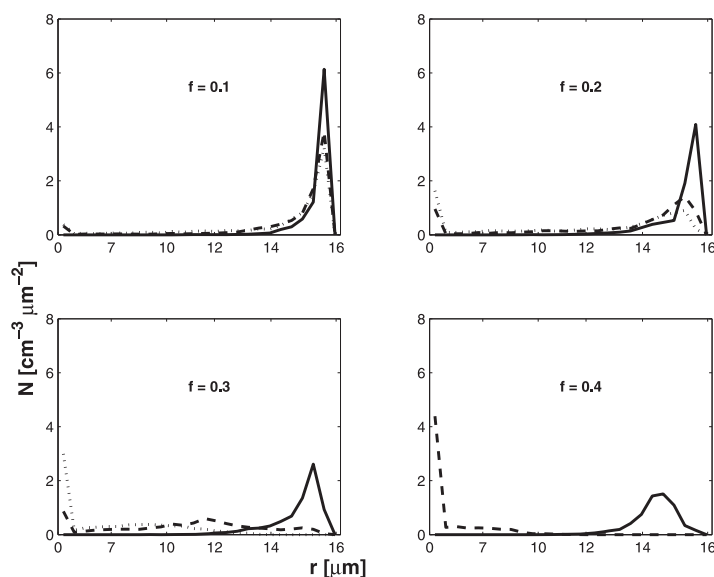
Figure 15. Droplet spectra for the control case ($RH_e = 0.87$, solid) compared to the reduced humidity cases ($RH_e = 0.44$, dashed and $RH_e = 0.22$, dotted) for entrained fractions $f = 0.1$, 0.2, 0.3, and 0.4. Two realizations for each case were averaged.

the dependence of σ_r on RH_e, N_e, and r_e will require further study.

5.7. Multiple Isobaric Entrainment Events

Figure 19 shows the DSD for the control case (solid) compared to that for multiple entrainment events (dashed) for isobaric mixing for the same "total" entrained air fractions ($f = 0.2$ and 0.4). For the multiple entrainment case the same fraction of air of $f = 0.1$ which corresponds to a blob of 2 m is always added. For example, before the second entrainment event the cloudy air has already mixed with the first entrainment fraction. So the difference is that in the multiple entrainment case the

newly entrained air fraction mixes with the cloudy parcel which is already mixed with environmental air. The sequence of entrainment events leads to a broader droplet spectrum at the higher entrained air fraction ($f = 0.4$).

6. Discussion and Conclusions

The EMPM simulates the evolving spatial structure due to entrainment and turbulent mixing down to the smallest turbulent scales and allows one to follow the history of each droplet. We used the EMPM to simulate the effects of entrainment and mixing on DSDs in ice-free cumuli. We investigated the evolution of DSDs after entrainment and isobaric mixing by varying several parameters including the entrained blob size, the turbulence dissipation rate, and the environmental relative humidity, for a range of entrained air fractions in a 20 m domain. Activation of cloud condensation nuclei in entrained air was not included in these simulations but could potentially play a role for ascending parcels [*Gerber*, 2006; *McFarlane and Grabowski*, 2007; *Bewley and Lasher-Trapp*, 2011].
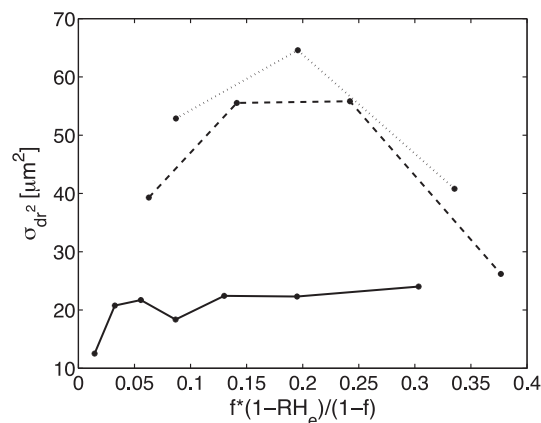

Figure 16. Droplet spectral width σ_{dr^2} of the control case $RH_e = 0.87$ (solid) and for reduced humidity cases $RH_e = 0.44$ (dashed) and $RH_e = 0.22$ (dotted) as a function of $f(1 - RH_e)$.

In the 20 m EMPM domain, the entrained air mixing fraction f was specified. However, the results are applicable to larger domains because the entrained blobs are broken down into a range of blob sizes that results in a range of entrained air fractions at the 20 m scale. Because mixing on scales larger than the 20 m domain size is relatively slow compared to that at sub-20 m scales, the DSDs in 20 m regions initially evolve independently.

A cumulus cloud entrains subsaturated air from its environment. Isobaric mixing of the cloudy air with the entrained air leads to a decrease of LWC and sometimes, but not always, a decrease of cloud droplet number concentration. Results of cloud resolving models show that large volumes of environmental air can be engulfed
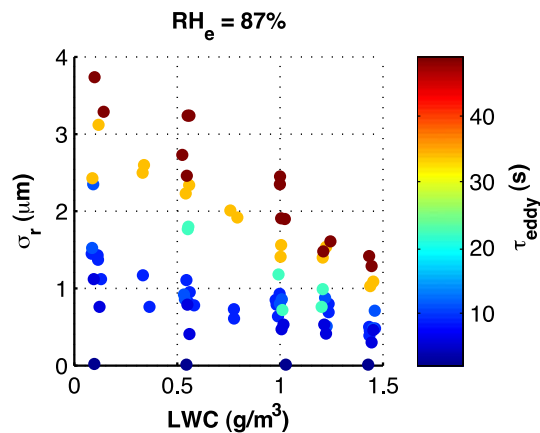
Figure 17. LWC versus σ_r, with τ_{eddy} indicated by the color, for all $RH_e = 0.87$ cases with $N_m > 0$.
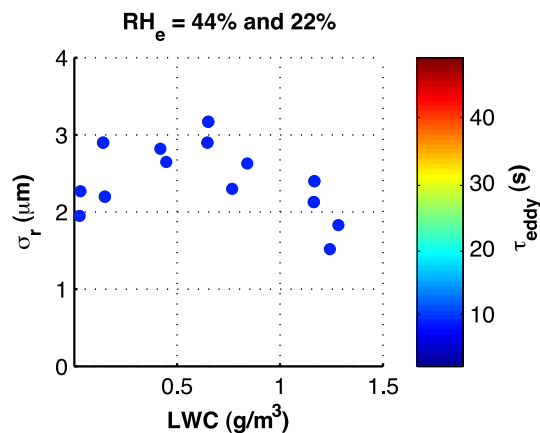

Figure 18. LWC versus σ_r, with τ_{eddy} indicated by the color, for all $RH_e = 0.44$ and 0.22 cases with $N_m > 0$.

deep into the cloud core [*Brenguier and Grabowski*, 1993]. However, the effects of entrainment and mixing on the number concentration and the droplet size distribution are not well understood and thus are difficult to predict. It is not feasible up to now with airborne microphysical measurements to isolate single entrainment-mixing events. The numerical modeling approach described in this study allows one to simulate the isobaric mixing of entrained air and its impact on the DSD.

We found that large turbulence dissipation rates and small entrained blob sizes produce rapid mixing that generally give the least broadening of the droplet spectrum. In such scenarios, the homogenization is so rapid that most of the droplets are exposed to a fairly uniform subsaturation field. With larger entrained blob sizes and smaller turbulence dissipation rates, mixing is slower. Such scenarios combined with a large drying potential of the entrained air (due to low humidity and/or large entrainment fraction) produced the broadest DSDs. In such cases, the droplet population experienced a wide range of subsaturation histories. Reducing the humidity of the entrained air or increasing the entrained blob size broadened the spectrum at smaller droplet radii, whereas lower dissipation rates enhanced broadening of the spectrum at both extremes of the DSD. The analysis of the time scales of these cases shows that broadening of the DSD is favored by relatively long mixing and short phase relaxation time scales (i.e., by Da $\gg$ 1). We also found that a sequence of isobaric entrainment events produces slightly greater DSD broadening than a single event with the same total entrained air fraction.

Our results demonstrate that it is possible to parameterize the broadening of the DSD due to entrainment and isobaric mixing, at least for a specific value of the relative humidity of the entrained air, as a function of the eddy mixing time scale and the LWC after mixing. In the EMPM simulations with $RH_e = 87$, the broadening of the DSD due to entrainment and mixing depends on τ_{eddy} and the LWC of the mixture, as shown in Figures 12, 14, and 17. However, from the limited number of EMPM simulations with $RH_e < 0.87$, we were unable to establish how the broadening depends in general on τ_{eddy} and the LWC (see Figures 15 and 18). Determining this
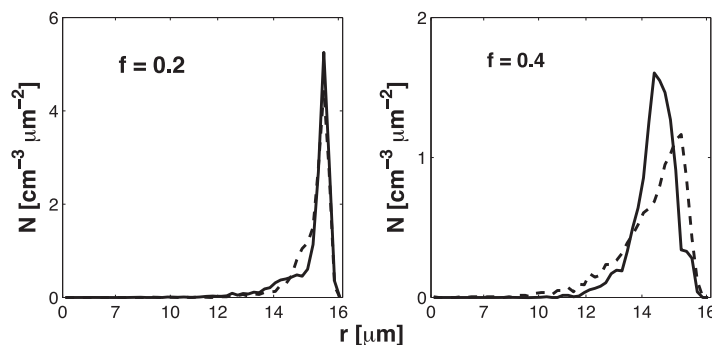

Figure 19. Comparison of the DSD of the control case (solid) with that of multiple entrainment events (dashed) for isobaric mixing for the same "total" entrained air fraction with $RH_e = 0.87$ for $f = 0.2$ and 0.4.

dependence is an important topic for future study. The comprehensive results obtained for $RH_e = 0.87$ should be extended to other values of RH_e, and also to other initial droplet sizes and concentrations.

Our results also suggest a new method for parameterizing the effects of entrainment and mixing on the droplet number concentration. We found that the fraction of droplets that totally evaporate increases as $r_m - \sigma_r$ decreases (Figure 6).

References

Andrejczuk, M., W. W. Grabowski, S. P. Malinowski, and P. K. Smolarkiewicz (2004), Numerical simulation of cloud-clear air interfacial mixing, *J. Atmos. Sci.*, *61*, 1726–1739.

Andrejczuk, M., W. W. Grabowski, S. P. Malinowski, and P. K. Smolarkiewicz (2006), Numerical simulation of cloud-clear air interfacial mixing: Effects on cloud microphysics, *J. Atmos. Sci.*, *63*, 3204–3225.

Baker, M. B., R. G. Corbin, and J. Latham (1980), The influence of entrainment on the evolution of cloud droplet spectra: I. A model of inhomogeneous mixing, *Q. J. R. Meteorol. Soc.*, *106*, 581–598.

Berry, E. X., and R. L. Reinhardt (1974), An analysis of cloud drop growth by collection: Part II. Single initial distributions, *J. Atmos. Sci.*, *31*, 1825–1831, doi:10.1175/1520-0469(1974)031<1825:AAOCDG>2.0.CO;2.

Bewley, J. L., and S. Lasher-Trapp (2011), Progress on predicting the breadth of droplet size distributions observed in small cumuli, *J. Atmos. Sci.*, *68*, 2921–2929, doi:10.1175/JAS-D-11–0153.1.

Blyth, A. M. (1993), Entrainment in cumulus clouds, *J. Appl. Meteorol.*, *32*, 626–641.

Brenguier, J. L. (1993), Observations of cloud microstructure at centimeter scale, *J. Atmos. Sci.*, *32*, 783–793.

Brenguier, J.-L., and W. W. Grabowsk (1993), Cumulus entrainment and cloud droplet spectra: A numerical model within a two-dimensional dynamical framework, *J. Atmos. Sci.*, *50*, 120–136.

Burnet, F., and J.-L. Brenguier (2007), Observational study of the entrainment-mixing process in warm convective clouds, *J. Atmos. Sci.*, *64*, 1995–2011.

Devenish, B. J., et al. (2012), Droplet growth in warm turbulent clouds, *Q. J. R. Meteorol. Soc.*, *138*, 1401–1429, doi:10.1002/qj.1897.

Gerber, H. (2006), Entrainment, mixing, and microphysics in RICO cumulus, in *12th Conferenec on Cloud Physics*, Am. Meteorol. Soc., Madison, Wis., paper 14.2A, https://ams.confex.com/ams/pdfpapers/109676.pdf.

Gerber, H. E., G. M. Frick, J. B. Jensen, and J. G. Hudson (2008), Entrainment, mixing, and microphysics in trade wind cumulus, *J. Meteorol. Soc. Jpn.*, *86A*, 87–106.

Grabowski, W. W. (1993), Cumulus entrainment, fine-scale mixing, and buoyancy reversal, *Q. J. R. Meteorol. Soc.*, *119*, 935–956.

Grabowski, W. W. (2007), Representation of turbulent mixing and buoyancy reversal in bulk cloud models, *J. Atmos. Sci.*, *64*, 3666–3680, doi:10.1175/JAS4047.1.

Jarecka, D., W. W. Grabowski, and H. Pawlowska (2009), Modeling of subgrid-scale mixing in large-eddy simulation of shallow convection, *J. Atmos. Sci.*, *66*, 2125–2133, doi:10.1175/2009JAS2929.1.

Jarecka, D., W. Grabowski, H. Morrison, and H. Pawlowska (2013), Homogeneity of the subgrid-scale turbulent mixing in large-eddy simulation of shallow convection, *J. Atmos. Sci.*, *70*, 2751–2767, doi:10.1175/JAS-D-13–042.1.

Jeffery, C. A., and J. M. Reisner (2006), A study of cloud mixing and evolution using PDF methods. Part I: Cloud front propagation and evaporation, *J. Atmos. Sci.*, *63*, 2848–2864.

Jensen, J. B., and M. B. Baker (1989), A simple model of droplet spectral evolution during turbulent mixing, *J. Atmos. Sci.*, *46*, 2812–2829.

Jensen, J. B., P. H. Austin, M. B. Baker, and A. M. Blyth (1985), Turbulent mixing, spectral evolution and dynamics in a warm cumulus cloud, *J. Atmos. Sci.*, *42*, 173–192, doi:10.1175/1520?0469(1985)042<0173:TMSEAD>2.0.CO;2.

Johnson, D. B. (1993), The onset of effective coalescence growth in convective clouds, *Q. J. R. Meteorol. Soc.*, *119*, 925–933.

Kerstein, A. R. (1988), A linear-eddy model of turbulent scalar trans-port and mixing, *Combust. Sci. Technol.*, *60*, 391–421.

Kerstein, A. R. (1991), Linear-eddy modeling of turbulent transport. Part 6, microstructure of diffuse scalar mixing fields, *Combust. Sci. Technol.*, *231*, 361–394.

Krueger, S. K., C.-W. Su, and P. McMurtry (1997), Modeling entrainment and finescale mixing in cumulus clouds, *J. Atmos. Sci.*, *54*, 2697–2712.

Kumar, B., J. Schumacher, and R. A. Shaw (2013), Cloud microphysical effects of turbulent mixing and entrainment, *Theor. Comput. Fluid Dyn.*, *27*(3-4), 361–376, doi:10.1007/s00162-012-0272-z.

Lasher-Trapp, S. G., W. A. Cooper, and A. M. Blyth (2005), Broadening of droplet size distributions from entrainment and mixing in a cumulus cloud, *Q. J. R. Meteorol. Soc.*, *131*, 195–220.

Lehmann, K., H. Siebert, and R. A. Shaw (2009), Homogeneous and inhomo-geneous mixing in cumulus clouds: Dependence on local turbulence structure, *J. Atmos. Sci.*, *66*, 3641–3659, doi:10.1175/2009JAS3012.1.

Lu, C., Y. Liu, S. Niu, S. K. Krueger, and T. Wagner (2013), Exploring parameterization for turbulent entrainment-mixing processes in clouds, *J. Geophys. Res. Atmos.*, *118*, 185–194, doi:10.1029/2012JD018464.

Magnussen, B. F., and B. H. Hjertager (1976), On mathematical modeling of turbulent combustion with special emphasis on soot formation and combustion, in *Proceedings of 16th International Symposium on Combustion*, pp. 719–729, Combust. Inst., Pittsburgh, Pa.

McFarlane, S. A., and W. W. Grabowski (2007), Optical properties of shallow tropical cumuli derived from ARM ground-based remote sensing, *Geophys. Res. Lett.*, *34*, L06808, doi:10.1029/2006GL028767.

Morrison, H., and W. W. Grabowski (2007), Comparison of bulk and bin warm-rain microphysics models using a kinematic framework, *J. Atmos. Sci.*, *64*, 2839–2861.

Raga, G. B., J. B. Jensen, and M. B. Baker (1990), Characteristics of cumulus band clouds off the coast of Hawaii, *J. Atmos. Sci.*, *47*, 338–355.

Rauber, R. M., et al. (2007), Rain in shallow cumulus over the ocean, *Bull. Am. Meteorol. Soc.*, *88*, 1912–1928.

Rogers, R. R., and M. K. Yau (1989), *A Short Course in Cloud Physics*, 3rd ed., Pergamon, Oxford, U. K.

Stevens, B., and G. Feingold (2009), Untangling aerosol effects on clouds and precipitation in a buffered system, *Nature*, *461*, 607–613, doi:10.1038/nature08281.

Stommel, H. (1947), Entrainment of air into a cumulus cloud, *J. Atmos. Sci.*, *4*, 91–94.

Su, C.-W., S. K. Krueger, P. A. McMurtry, and P. H. Austin (1998), Linear eddy modeling of droplet spectral evolution during entrainment and mixing in cumulus clouds, *Atmos. Res.*, *47–48*, 41–58.